


Efficient treatment of low-frequency response and decoherence in a real-time evolution schemeXiurong Feng and Feng Wang *School of Physics, Beijing Institute of Technology, Beijing 100081, China*

(Received 13 December 2021; accepted 15 April 2022; published 5 May 2022)

In this paper, we present an improved real-time current-based approach for calculating the frequency-dependent dielectric function of a bulk periodic system, which can achieve a unified treatment of longitudinal and transverse macroscopic geometries on the same footing, and an improvement to make the approach of calculating dielectric function more robust for the avoidance of numerical divergencies at low frequency near zero in some specific cases. The validity of the improved approach implementation is verified by calculating the dielectric function of bulk periodic system in the ground in the longitudinal geometry, enabling the improved approach to be extended to excited bulk periodic systems in the transverse geometry. Further, a phenomenological description of decoherence has been incorporated within the framework of time-dependent density-functional theory (TDDFT). It is concluded that the decoherence model can suppress the numerical divergence of low frequency and grows the excitonic feature of silicon, although it adopts the approximate time-dependent exchange-correlation potential. Thus, the use of the decoherence TDDFT model opens pathways for handling the decoherence effects within the framework of TDDFT.

DOI: [10.1103/PhysRevE.105.055303](https://doi.org/10.1103/PhysRevE.105.055303)**I. INTRODUCTION**

The frequency-dependent dielectric function is typically required for characterizing the optical properties of the bulk periodic system. TDDFT has been used extensively for calculating the frequency-dependent dielectric function of various bulk periodic systems, including metals [1–3], semiconductors [4–8], and insulators [1,9–14], both in its frequency and in its real-time form. From the theoretical point of view [15–17], the approaches for calculating the longitudinal macroscopic dielectric function can be divided into two classes, namely, the density-based and the current-based approach, and each one has its own set of advantages and disadvantages. We note that, in some specific cases, formal equivalence of the two approaches does not guarantee numerical equivalence in practical calculations. Generally speaking, compared with the density-based approaches, the current-based approaches are more general but more susceptible to numerical issues and instabilities.

As explained in Ref. [1], a real-time current-based approach has been derived by Bertsch *et al.*, in which the entire frequency-dependent dielectric function can be calculated from a single real-time evolution of the system perturbed by an impulsive external vector potential field $\mathbf{A}_{\text{ext}}(t) = \mathbf{A}_0\theta(t)$, where $\theta(t)$ is the Heaviside step function, corresponding to the impulsive external electric field, $\mathbf{E}_{\text{ext}}(t) = -(1/c)[d\mathbf{A}_{\text{ext}}(t)/dt] = -(1/c)\mathbf{A}_0\delta(t)$. Apart from the significant increase of computational efficiency, a numerical advantage of the approach of Bertsch *et al.* combined with TDDFT is that it avoids the explicit calculation of the extra more complicated exchange-correlation kernel involved in

most of the approaches to linear response in TDDFT [18], and hence it is suitable for bulk periodic systems where the underlying static density is extended.

We note that there are several calculations of the dielectric function employing the approach derived by Bertsch *et al.* in either the longitudinal or transverse geometry [1,4,10–12,19–26]. In the transverse geometry, the total vector potential field \mathbf{A}_{tot} in the system Hamiltonian simply is external vector potential field \mathbf{A}_{ext} . In the longitudinal geometry, $\mathbf{A}_{\text{tot}} = \mathbf{A}_{\text{ext}} + \mathbf{A}_{\text{ind}}$, where \mathbf{A}_{ind} is the field from the induced current in the system. Although it has been argued [23] that as a means to calculate dielectric functions on both geometry choices give the same results, it should be noted that there is indeed a spurious divergency at low frequency near zero in the calculated dielectric function in some specific cases for insulators. The divergence in the calculations of the real-time current-based approach originates from the fact that they applied a constant damping as postprocessing in the velocity gauge, and this is not fairly exact, because damping in this gauge is field dependent and cannot be simply applied at the end of the calculations or at least not so straightforwardly.

As is well known, the predictive power of TDDFT is subject to the accuracy of the approximations made in two essential ingredients, namely, the time-dependent exchange-correlation (XC) potential and the functional for the physical observables, excluding numerical approximations that are normally controllable. In practice, it needs approximations for the accurate time-dependent XC potential with nonlocality in space and time and the property of derivative discontinuity. So far, the general applications of TDDFT do not consider discontinuity and completely depend on adiabatic approximation, which feeds the instantaneous time-dependent density into the known static XC potential of the static density functional theory (SDFT). However, it is not clear whether the

*wangfeng01@tsinghua.org.cn

more accurate XC potential in SDFT is necessarily related to the improvement described in TDDFT. Many benchmark studies have explored the performance of calculations in TDDFT using static XC potentials within the adiabatic approximation. Most benchmark studies are mainly limited to the range of linear and perturbative response, where TDDFT is an effective standard time-dependent perturbation theory. Even with the accurate time-dependent XC potential, from a practical viewpoint of real-time TDDFT models, there is still a question is how to describe the effect of decoherence caused by the electron-electron collisions, emission of photons, and electron-phonon scattering, and so on. There are many alternate methods. The possible influence of decoherence, for example, can be included by applying a purely phenomenological approach employing damping constants [27] or the quantum friction approach [28].

In this paper, a phenomenological description of decoherence has been incorporated within the framework of TDDFT. For demonstrating the validity of the decoherence TDDFT model, we conduct a numerical study on an improved real-time current-based approach for calculating the frequency-dependent dielectric function of a bulk periodic system, taking diamond and silicon as the concrete examples. In addition, it is worth noting that this paper puts forward a unified treatment of longitudinal and transverse macroscopic geometries on the same footing for the avoidance of numerical divergencies at low frequency near zero in some specific cases by introducing the polarization density $\mathbf{P}(t)$.

The paper is organized as follows. In Sec. II, we provide concepts and formulas of deriving a dielectric function and our formalism of an improved real-time current-based approach for the dielectric function of bulk periodic system, followed by the real-time TDDFT formalism underlying the time evolution of the vector potential and the current density in periodic systems with allowance for a phenomenological description of decoherence. In Sec. III we compute the dielectric functions as examples for diamond and silicon in ground state comparing the results of our improved approach with the experiments, followed by conclusions in Sec. IV.

II. METHOD

A. The calculation formulas of dielectric function

In the linear response regime, the dielectric permittivity $\varepsilon_{m,n}(\omega)$ can be expressed by the conductivity $\sigma_{m,n}(\omega)$ [14],

$$\varepsilon_{m,n}(\omega) = \delta_{m,n} + \frac{4\pi i \sigma_{m,n}(\omega)}{\omega}, \quad (1)$$

where m and n indicate Cartesian component ($m, n = x, y, z$). In the following we outline some of the formulas utilized in the derivation of Eq. (1). On the one hand, in the frequency domain, $\varepsilon(\omega)$ can be strictly determined by the following equations:

$$\begin{aligned} \mathbf{D}(\omega) &= \varepsilon(\omega) \mathbf{E}_{\text{tot}}(\omega), \\ \mathbf{D}(\omega) &\equiv \mathbf{E}_{\text{tot}}(\omega) + 4\pi \mathbf{P}(\omega), \\ \mathbf{j}(\omega) &= \sigma(\omega) \mathbf{E}_{\text{tot}}(\omega), \\ -i\omega \mathbf{P}(\omega) &= \mathbf{j}(\omega), \end{aligned} \quad (2)$$

where $\mathbf{D}(\omega)$ is the electric displacement field, $\mathbf{E}_{\text{tot}}(\omega)$ is the total electric field, and $\mathbf{P}(\omega)$ is the polarization density. On the other hand, in the time domain, $\varepsilon(\omega)$ can also be expressed by the following equations:

$$\begin{aligned} \int dt e^{i\omega t} \mathbf{D}(t) &= \varepsilon(\omega) \int dt e^{i\omega t} \mathbf{E}_{\text{tot}}(t), \\ \mathbf{D}(t) &= -\frac{1}{c} \frac{d\mathbf{A}_{\text{ext}}(t)}{dt}, \\ \mathbf{A}_{\text{tot}}(t) &= \mathbf{A}_{\text{ext}}(t) + \mathbf{A}_{\text{ind}}(t), \\ \mathbf{E}_{\text{ind}}(t) &= -4\pi \mathbf{P}(t), \\ \frac{d\mathbf{P}(t)}{dt} &= \mathbf{j}(t), \\ \mathbf{E}(t) &= -\frac{1}{c} \frac{d\mathbf{A}(t)}{dt}, \\ \frac{d^2 \mathbf{A}_{\text{ind}}(t)}{dt^2} &= 4\pi c \mathbf{j}(t), \\ \int dt e^{i\omega t} \mathbf{j}(t) &= \sigma(\omega) \int dt e^{i\omega t} \mathbf{E}_{\text{tot}}(t). \end{aligned} \quad (3)$$

In the longitudinal geometry, the total field $\mathbf{E}_{\text{tot}}(t)$ is given by the sum of the external field $\mathbf{E}_{\text{ext}}(t)$ and the induced field $\mathbf{E}_{\text{ind}}(t)$ in a geometry of a thin film [1,9,19,23,24]. Correspondingly, the dielectric function $\varepsilon_{m,n}(\omega)$ can be expressed in terms of the vector potential,

$$\begin{aligned} \frac{1}{\varepsilon_{m,n}(\omega)} &= \frac{\int_0^{+\infty} dt e^{i\omega t} \frac{d\mathbf{A}_{\text{tot},m}(t)}{dt}}{\int_0^{+\infty} dt e^{i\omega t} \frac{d\mathbf{A}_{\text{ext},n}(t)}{dt}} \\ &= \delta_{m,n} + \frac{\int_0^{+\infty} dt e^{i\omega t} \frac{d\mathbf{A}_{\text{ind},m}(t)}{dt}}{\int_0^{+\infty} dt e^{i\omega t} \frac{d\mathbf{A}_{\text{ext},n}(t)}{dt}}. \end{aligned} \quad (4)$$

To extract the dielectric properties of excited matter, the numerical pump-probe experiment is carried out [6]. Here the Heaviside step function [1], $\mathbf{A}_{\text{ext}}^{\text{probe}}(t) = \mathbf{A}_0 \theta(t)$, is applied as a probe external vector potential, corresponding to the probe external electric field, $\mathbf{E}_{\text{ext}}^{\text{probe}}(t) = -(1/c)[d\mathbf{A}_{\text{ext}}^{\text{probe}}(t)/dt] = -(1/c)\mathbf{A}_0 \delta(t)$. It is assumed that the probe pulse is weak enough to ignore all nonlinear processes involving more than one photon, so \mathbf{A}_0 takes a small value of 1 a.u. The induced vector potential $\mathbf{A}_{\text{ind}}^{\text{probe}}(t)$ is the difference between $\mathbf{A}_{\text{ind}}^{\text{pump+probe}}(t)$ containing both pump and probe pulses and $\mathbf{A}_{\text{ind}}^{\text{pump}}(t)$ containing the pump pulse only,

$$\mathbf{A}_{\text{ind}}^{\text{probe}}(t) = \mathbf{A}_{\text{ind}}^{\text{pump+probe}}(t) - \mathbf{A}_{\text{ind}}^{\text{pump}}(t). \quad (5)$$

For the case of $m = n$, the dielectric function can be expressed as

$$\frac{1}{\varepsilon_{m,m}(\omega)} = 1 + \frac{1}{\mathbf{A}_{0,m}} \int_0^{+\infty} dt e^{i\omega t} \frac{d\mathbf{A}_{\text{ind},m}^{\text{probe}}(t)}{dt}. \quad (6)$$

In practical application, time evolution is carried out in a finite period T . According to the uncertainty principle $\Delta E \sim h/T$, the energy resolution of spectrum ΔE obtained with a Fourier transform is interrelated to time period T . In $\mathbf{A}_{\text{ind},m}^{\text{probe}}(t)$, the transitions to the bound excited state show an oscillation, which persists without any damping. Due to a sharp cutoff of the integrand at end of the time-evolution

period T in the Fourier transformation, it is accompanied by wiggles around the excitation energy. The introduction of damping function into the Fourier transform can eliminate the wiggles to some extent [10,11,19,21,22,24,25]. Here a simple choice of damping function is to contain a small imaginary part $i\gamma$ in frequency ω , which is equivalent to multiplying the Fourier transform of Eq. (6) by the damping function [24]

$$f(t) = e^{-\gamma t}. \quad (7)$$

If the time evolution lasts long period enough, it gives a Lorentzian line shape to the bound transitions. As a result, the snapshot of the dielectric function $\varepsilon_{m,m}(\omega)$ of matter is given by

$$\frac{1}{\varepsilon_{m,m}(\omega)} = 1 + \frac{1}{\mathbf{A}_{0,m}} \int_0^T dt e^{i\omega t - \gamma t} \frac{d\mathbf{A}_{\text{ind},m}^{\text{probe}}(t)}{dt}, \quad (8)$$

or

$$\frac{1}{\varepsilon_{m,m}(\omega)} = 1 + i \frac{4\pi c \int_0^T dt e^{i\omega t - \gamma t} \mathbf{j}_m^{\text{probe}}(t)}{\omega \mathbf{A}_{0,m}}. \quad (9)$$

As a consequence, a finite width of the peaks at the imaginary part of the dielectric function can be obtained, which mimics the experimental broadening of the spectrum from a physical point of view [25].

In the transverse geometry, there is no surface charge in the material, and the induced polarization field does not contribute to the electric field in the cell [23]. The total vector potential field $\mathbf{A}(t)$ is provided only by external vector potential field $\mathbf{A}_{\text{ext}}^{\text{probe}}$. Therefore, in the linear response regime, the frequency-dependent dielectric function $\varepsilon(\omega)$ is given by the current density [6,19,22,23],

$$\varepsilon_{m,m}(\omega) = 1 - i \frac{4\pi c \int_0^T dt e^{i\omega t - \gamma t} \mathbf{j}_m^{\text{probe}}(t)}{\omega \mathbf{A}_{0,m}}, \quad (10)$$

where the induced current density $\mathbf{j}^{\text{probe}}(t)$ is defined as the difference between $\mathbf{j}^{\text{pump}+\text{probe}}(t)$ containing both pump and probe pulses and $\mathbf{j}^{\text{pump}}(t)$ containing the pump pulse only,

$$\mathbf{j}^{\text{probe}}(t) = \mathbf{j}^{\text{pump}+\text{probe}}(t) - \mathbf{j}^{\text{pump}}(t). \quad (11)$$

B. The improved approach of dielectric function by introducing polarization density

Since frequency ω is in the denominator in Eq. (10), it is more susceptible to numerical issues and instabilities at around $\omega = 0$. It is noted that in some specific cases, there are indeed numerical divergencies at vanishing frequency in the calculated dielectric function, which causes the numerical divergencies and destroys the low-frequency behavior of the dielectric function [6,19]. In the frequency domain, there are several solutions to avoid numerical divergence at low frequency [15,29–31], such as correctly including the smearing by redefining the dielectric function and the conductivity sum rule [15,29]. Further, the calculation in frequency domain always needs a truncated set of bands, which makes the Thomas-Reiche-Kuhn sum rule not exactly satisfied, resulting in some problems such as the divergence of linear polarization response at the low-frequency limit [30,31]. In this paper, we calculate the dielectric function in the time domain. In order

to avoid the numerical divergencies at low frequency near zero in some specific cases, we make a small improvement by introducing the polarization density $\mathbf{P}(t)$, which uniformly treats longitudinal and transverse macroscopic geometries on the same footing.

In the longitudinal geometry, the dielectric function $\varepsilon(\omega)$ is obtained as follows:

$$\begin{aligned} \varepsilon_{m,m}(\omega) &= 1 + i \frac{4\pi \sigma_{m,m}(\omega)}{\omega} \\ &= 1 + i \frac{4\pi \int_0^T dt e^{i\omega t - \gamma t} \mathbf{j}_m(t)}{\omega \int_0^T dt e^{i\omega t - \gamma t} \mathbf{E}_{\text{tot},m}(t)} \\ &= 1 + i \frac{-4\pi c \int_0^T dt e^{i\omega t - \gamma t} \frac{d\mathbf{P}_m(t)}{dt}}{\omega \left(\int_0^T dt e^{i\omega t - \gamma t} \frac{d\mathbf{A}_{\text{ind},m}}{dt} dt + \int_0^T dt e^{i\omega t - \gamma t} \frac{d\mathbf{A}_{\text{ext},m}}{dt} dt \right)} \\ &= 1 + i \frac{-4\pi c \int_0^T dt e^{i\omega t - \gamma t} \frac{d\mathbf{P}_m(t)}{dt}}{\omega \left(\mathbf{A}_{0,m} + 4\pi c \int_0^T dt e^{i\omega t - \gamma t} \mathbf{P}_m(t) dt \right)} \\ &= 1 - \frac{4\pi c \int_0^T dt e^{i\omega t - \gamma t} \mathbf{P}_m(t) dt}{\mathbf{A}_{0,m} + 4\pi c \int_0^T dt e^{i\omega t - \gamma t} \mathbf{P}_m(t) dt}. \end{aligned} \quad (12)$$

In the transverse geometry, it is expressed as

$$\begin{aligned} \varepsilon_{m,m}(\omega) &= 1 + \frac{4\pi i \sigma_{m,m}(\omega)}{\omega} \\ &= 1 + i \frac{4\pi \int_0^T dt e^{i\omega t - \gamma t} \mathbf{j}_m(t)}{\omega \int_0^T dt e^{i\omega t - \gamma t} \mathbf{E}_{\text{tot},m}(t)} \\ &= 1 + i \frac{-4\pi c \int_0^T dt e^{i\omega t - \gamma t} \frac{d\mathbf{P}_m(t)}{dt}}{\omega \int_0^T dt e^{i\omega t - \gamma t} \frac{d\mathbf{A}_{\text{tot},m}}{dt} dt} \\ &= 1 + i \frac{-4\pi c \int_0^T dt e^{i\omega t - \gamma t} \frac{d\mathbf{P}_m(t)}{dt}}{\omega \mathbf{A}_{0,m}} \\ &= 1 - \frac{4\pi c \int_0^T dt e^{i\omega t - \gamma t} \mathbf{P}_m(t) dt}{\mathbf{A}_{0,m}}. \end{aligned} \quad (13)$$

C. The improved real-time TDDFT formalism with allowance for the decoherence

The TDDFT has proven to be the applications in the linear response that can be treated as a perturbation and the nonlinear and nonperturbative electron dynamics induced by an intense laser pulses [24,32,33]. It can also describe the periodic system by both density and the current density [34,35]. In view of the good experience with TDDFT, we describe the electron dynamics based on real time and real space of TDDFT.

Here we briefly recapitulate the framework of the TDDFT. The details have been accounted for elsewhere [10–12]. The motion of electrons is described by the time-dependent Kohn-Sham (TDKS) equation,

$$i\hbar \frac{\partial}{\partial t} \psi_i(\mathbf{r}, t) = \hat{H}_{KS}(\mathbf{r}, t) \psi_i(\mathbf{r}, t), \quad (14)$$

where $\psi_i(\mathbf{r}, t)$ is the single-particle orbital and \hat{H}_{KS} is the time-dependent Kohn-Sham Hamiltonian defined by

$$\hat{H}_{KS}(\mathbf{r}, t) = \frac{1}{2m_e} \left(-i\hbar \nabla + \frac{e}{c} \mathbf{A}_{\text{tot}} \right)^2 + V_{\text{tot}}, \quad (15)$$

where m_e is the effective mass of electrons, e is an elementary charge ($e > 0$), c is the scalar velocity of light in vacuum and \mathbf{A}_{tot} is the total vector potential. Since we apply a time-dependent, spatially uniform electric field $\mathbf{E}(t)$, the vector potential $\mathbf{A}(t)$ is described by $\mathbf{A}(t) = -c \int^t dt' \mathbf{E}(t')$. In addition, the time-dependent total scalar potential V_{tot} is given as follows:

$$V_{tot}(\mathbf{r}, t) = V_{ion}(\mathbf{r}, t) + \int d\mathbf{r}' \frac{n(\mathbf{r}', t)e^2}{|\mathbf{r}' - \mathbf{r}|} + V_{XC}(\mathbf{r}, t), \quad (16)$$

where $n(\mathbf{r}', t) = 2 \sum_i |\psi_i(\mathbf{r}', t)|^2$ is the valence electron density related to the orbital, the factor of 2 indicates that each orbital is fully occupied, V_{ion} is the norm-conserving pseudopotentials to deal with the interaction between valence electrons and the ionic core, considering only valence electron orbitals [36], and V_{XC} is the XC potential, adopting the adiabatic approximation.

In the longitudinal geometry, considering the surface charge effect, i.e., charging the dielectric interface within a limited distance, the induced potential \mathbf{A}_{ind} is generated. The induced field \mathbf{A}_{ind} can also be written as $\mathbf{A}_{ind} = \mathbf{A}_{EM} + \mathbf{A}_{XC}$, where \mathbf{A}_{EM} is the full electromagnetic potential and \mathbf{A}_{XC} is the macroscopic exchange-correlation field. In the present work, all macroscopic components of the exchange-correlation contribution are neglected [20]. We use the full electromagnetic potential \mathbf{A}_{EM} and the scalar potential $\phi(\mathbf{r}, t)$ to describe the propagation of the electromagnetic fields. They satisfy the microscopic Maxwell equations [19,37,38]. In the Coulomb gauge, we have the following equations:

$$\left(\frac{1}{c^2} \frac{\partial^2}{\partial t^2} - \nabla^2 \right) \mathbf{A}_{EM}(\mathbf{r}, t) + \frac{1}{c} \frac{\partial}{\partial t} \nabla \phi(\mathbf{r}, t) = \frac{4\pi}{c} \mathbf{j}(\mathbf{r}, t), \quad (17)$$

where $\mathbf{j}(\mathbf{r}, t)$ is the electric current density, given by

$$\mathbf{j}(\mathbf{r}, t) = -2e \sum_i \text{Re} [\psi_i^*(\mathbf{r}, t) \hat{\mathbf{v}} \psi_i(\mathbf{r}, t)], \quad (18)$$

where $\hat{\mathbf{v}}$ is the velocity operator [6,20],

$$\hat{\mathbf{v}} = \frac{1}{i\hbar} [\hat{\mathbf{r}}, \hat{H}_{KS}]. \quad (19)$$

In addition, the $\phi(\mathbf{r}, t)$ satisfies the Poisson equation,

$$\nabla^2 \phi(\mathbf{r}, t) = -4\pi \rho(\mathbf{r}, t), \quad (20)$$

where $\rho(\mathbf{r}, t)$ is the charge density composed of ionic and electronic contributions. Considering that the length scale of the electron dynamics is much less than the wavelength of the optical electric field with visible or infrared frequencies in a crystalline solid [14], we employ dipole approximation and apply a coarse-graining approximation of \mathbf{A}_{EM} , \mathbf{j} , and ϕ to be spatially uniform, leading to

$$\frac{d^2 \mathbf{A}_{EM}(t)}{dt^2} = 4\pi c \mathbf{j}(t). \quad (21)$$

Here we consider a phenomenological description of decoherence, and accordingly the relationship between $\mathbf{P}(t)$ and $\mathbf{j}(t)$ can be represented as [39]

$$\frac{d\mathbf{P}(t)}{dt} + \beta \mathbf{P}(t) = \mathbf{j}(t), \quad (22)$$

where β is characteristic relaxation rate. In order to write a closed set of equations, Eq. (22) is expressed as follows by an induced vector potential $\mathbf{A}_{ind}(t)$, which is related to the polarization by $\mathbf{P}(t) = (1/4\pi c)[d\mathbf{A}_{ind}(t)/dt]$,

$$\frac{d^2 \mathbf{A}_{ind}(t)}{dt^2} + \beta \frac{d\mathbf{A}_{ind}(t)}{dt} = 4\pi c \mathbf{j}(t). \quad (23)$$

In the present article, our simulations are carried out with OCTOPUS code (version 10.5) [40,41] which we modified to introduce Eq. (23). In addition, we adopt the generalized gradient approximation (GGA) based on the Perdew-Burke-Ernzerhof functional (PBE) in our calculation [42].

III. APPLICATIONS

In this section, taking bulk diamond and silicon crystals as examples, we calculate the dielectric functions by the decoherence TDDFT model, compared with the experimental results. Atomic units (a.u.) are used throughout unless stated otherwise. The periodicity of diamond crystal is simulated by using a cubic cell with lattice parameter of $a = 6.74$ a.u. under the periodic boundary condition. The cubic unit cell contains eight carbon atoms. The TDKS equation is solved in a discretized three-dimensional space mesh, which is discretely into $20 \times 20 \times 20$ grid points with a grid spacing of 0.34 a.u. The first Brillouin zone in the inverted space is discretized with $8 \times 8 \times 8$ k points. For silicon crystal, a cubic unit cell including eight silicon atoms with a lattice parameter of 10.26 a.u. is used to simulate the periodicity. The grid is discretely into $30 \times 30 \times 30$ grid points with a grid spacing of 0.34 a.u. The number of k points is taken as $12 \times 12 \times 12$. Moreover, the time-dependent evolution of the Kohn-Sham equation adopts the enforced time-reversed symmetric method [43] with a time-dependent evolution time step of 0.01 a.u.

To investigate the dielectric function of dielectric material, we use a weak probe pulse as the external potential. The evolution time of probe pulse is 200 a.u. to ensure that the spectrum with enough resolution can be acquired with a Fourier transform. Moreover, in order to better simulate the experimental results, in our research, we choose a suitable damping factor $\gamma = 0.025$ in longitudinal geometry, while the damping factor γ is chosen to be 0.015 in the transverse geometry for diamond crystal. For silicon crystal, we choose a damping factor $\gamma = 0.007$ in longitudinal geometry.

First, in order to verify the validity of the improvement by introducing polarization density, we compare the results of the dielectric function in bulk diamond at the ground state by different numerical approaches. Figure 1 shows the real (upper panel) and imaginary part (bottom panel) of the frequency-dependent dielectric function $\varepsilon(\omega)$ of diamond at ground state in longitudinal geometry through Eqs. (8), (9), and (12), respectively. For comparison, the experimental dielectric function of diamond is displayed with dark gray circle in panel. In Fig. 1 it is found that the real and imaginary parts of $\varepsilon(\omega)$ from Fourier transforming of $d\mathbf{A}_{ind}(t)/dt$ in Eq. (8) and $\mathbf{P}(t)$ in Eq. (9), respectively, show good agreement, while from Fourier transforming of $\mathbf{j}(t)$ in Eq. (12), the real of $\varepsilon(\omega)$ tends to zero in the $\omega \rightarrow 0$ limit, and the peak value of real part and imaginary part is lower.

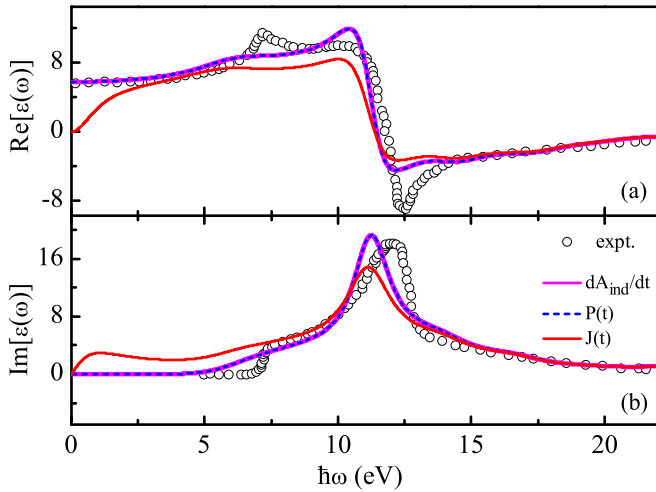


FIG. 1. In the longitudinal geometry, the real (upper panel) and imaginary parts (bottom panel) of the frequency-dependent dielectric function $\varepsilon(\omega)$ of diamond at ground state are plotted by three numerical approaches. The experimental dielectric function of diamond is displayed in a dark gray circle [44].

Also, in the transverse geometry, the real [corresponding to Fig. 2(a)] and imaginary part [corresponding to Fig. 2(b)] of the dielectric function $\varepsilon(\omega)$ of diamond at ground state from two numerical approaches are plotted in Fig. 2, compared with measured values in a dark gray circle. We find that the real and imaginary parts of $\varepsilon(\omega)$ from Fourier transforming of $\mathbf{j}(t)$ in Eq. (10) and $\mathbf{P}(t)$ in Eq. (13), respectively, show reasonably good agreement except near $\omega = 0$. As discussed in Ref. [19,22], we observe divergent behavior in the $\omega \rightarrow 0$ limit of the dielectric function $\varepsilon(\omega)$ from Fourier transforming $\mathbf{j}(t)$, due to the division of Eq. (10) by frequency $\omega = 0$. However, the small improvement by introducing the polarization density $\mathbf{P}(t)$ can well avoid the numerical divergencies at low frequency near zero. In addition, by introducing polarization

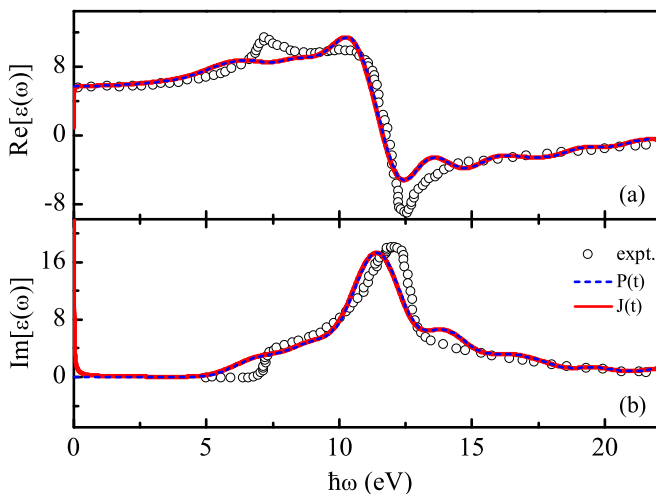


FIG. 2. In the transverse geometry, the real (upper panel) and imaginary parts (bottom panel) of the frequency-dependent dielectric function $\varepsilon(\omega)$ of diamond at ground state are shown with two numerical approaches, compared with measured values [44].

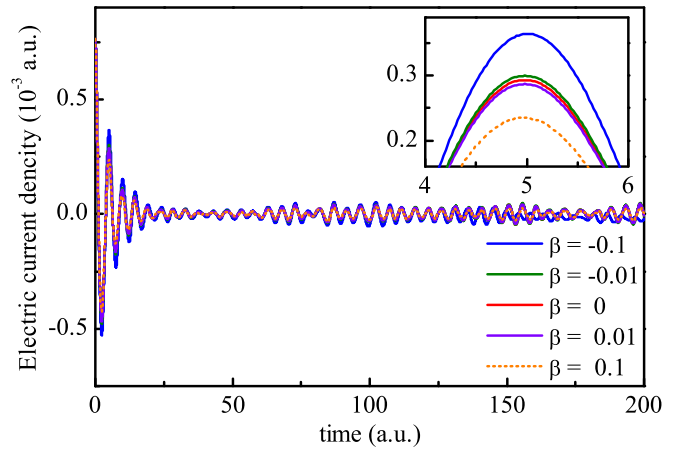


FIG. 3. In the longitudinal geometry, after the delta-function distortion is applied at $t = 0$, the electric current density distribution corresponding to different characteristic relaxation rate β in crystalline diamond. For convenience of observation, the illustration shows a partial enlarged view.

density, the longitudinal and transverse macroscopic geometries are treated uniformly on the same footing.

In the next section, a phenomenological relaxation is introduced in the equation motion for the induced vector potential, reflecting surface charge, within the longitudinal geometry. The dielectric function of dielectric materials is studied with allowance for the decoherence TDDFT model under the longitudinal geometry. Taking diamond as an example, the electric current density distribution as functions of time is given in Fig. 3, corresponding to a different characteristic relaxation rate β , respectively. All electric currents coincide with each other accurately at $t = 0$, since the initial current is determined by the summation rule[1], and then starts to depart. As seen from Fig. 3, we can also find that the larger β is, the smaller the amplitude of current oscillation becomes. With allowance for the decoherence TDDFT model, Fig. 4 further shows the dielectric function of diamond crystal as a function of frequency under a different characteristic relaxation rate β : the real part in Fig. 4(a) and the imaginary part in Fig. 4(b). It can be seen from Fig. 4 that for diamond, the dielectric functions corresponding to the negative value of β coincide with each other, which is consistent with the case without considering decoherence. For the positive value of β , the peak value of the imaginary part of the dielectric function is higher, and the peak position is shifted to the high-energy direction compared with the result without decoherence, which is closer to the experimental result.

Then, considering that the silicon crystal has an excitonic peak, i.e., the interaction of an electron in the conduction band with the hole left behind in the valence band, we numerically study the influence of the decoherence TDDFT model on its dielectric function. At present, for the so-called exciton effect, this problem has been treated by some authors [46,47] by using the state-of-the-art methods, such as the GW approximation of electron self-energy and the Bethe-Salpeter equation of electron-hole interaction. However, these methods have high requirements for calculation and are not easy to adapt to the emerging new generation of electronic materials.

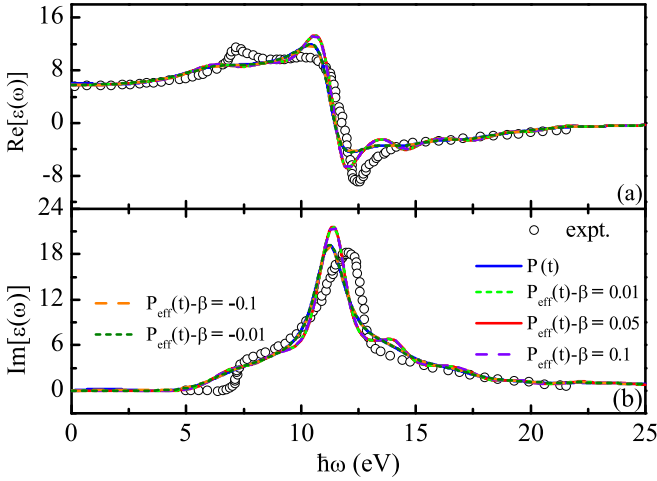


FIG. 4. In the longitudinal geometry, the real (upper panel) and imaginary parts (bottom panel) of the frequency-dependent dielectric function $\varepsilon(\omega)$ of diamond at ground state are plotted by a different characteristic relaxation rate β . The experimental dielectric function of diamond is displayed in a dark gray circle [44].

Within the framework of TDDFT, the standard method based on the adiabatic local density approximation (ALDA) [48] greatly underestimates the excitonic peak of a low-energy peak in the spectrum. Improvements to the ALDA, such as the GGA, have not fared much better. Recently, several new methods have been proposed to accurately describe the excitonic effect in the frequency domain; for example, Nazarov *et al.* [7] developed the adiabatic TDDFT formalism for the kinetic energy-dependent (MGGA) XC functionals, Sharma *et al.* [49] proposed a bootstrap method of a new parameter-free approximation for the TDDFT XC kernel which is solved from a self-consistent procedure, Trevisanutto *et al.* [50] proposed a static approximation to the XC kernel based on the jellium-with-gap model, Cavo *et al.* [51] proposed the pure kernel which combines the derivative discontinuity and the polarization functional, and Berger *et al.* [52] presented a fully parameter-free density-functional approach using a simple dynamical polarization functional. In this paper, with allowance for the decoherence TDDFT model of real-time methods based on the GGA, we calculated the dielectric function as a function of frequency of silicon crystals at different β in Fig. 5. Surprisingly, it is found that the decoherence TDDFT model greatly improves the results of the dielectric function of silicon crystals, and the exciton effect in silicon can be captured to some extent in the frequency space. In particular, the excitonic peak is considerably more pronounced at $\beta = 0.03$, but slightly underestimates the intensity of the first excitonic peak. Moreover, for the negative value of β , the dielectric function is close to the result without considering decoherence, and it is also consistent with the result when the positive value of β is relatively small, such as $\beta = 0.01$. We also note that the divergence of the dielectric function at low frequencies is obviously suppressed with allowance for the decoherence TDDFT model, and the dielectric constant is in good agreement with the empirical value. Also, real and imaginary parts of the dielectric function look to shift towards a lower frequency in comparison with the experimental value,

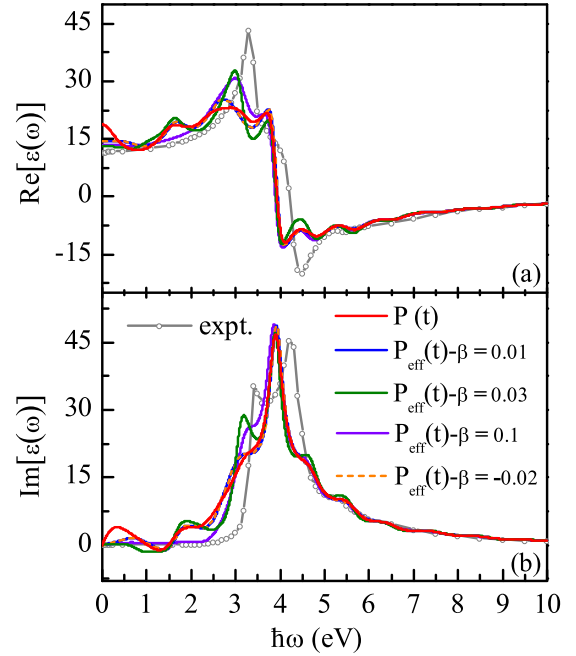


FIG. 5. In the longitudinal geometry, the real (upper panel) and imaginary parts (bottom panel) of the frequency-dependent dielectric function $\varepsilon(\omega)$ of silicon at ground state are plotted by a different characteristic relaxation rate β . The experimental dielectric function of silicon is displayed in a dark gray circle [7,45].

and the corresponding energy difference between the two peaks of the imaginary part is consistent with the measured value. This may be because of the well-known underestimation of the bandgap energy in the GGA. Actually, we do not expect the model and the experiment to be consistent in quantity due to the influence of the exciton effects in silicon. To do this, we would need to use the accurate time-dependent XC potential and the correct atomic pseudopotentials with correct bound and excited states. The present TDDFT results are thus not meant for a quantitative comparison with experiment. Although all the complex mechanisms are not fully accounted for the TDDFT at the PBE level, our purpose is to clarify the effect with allowance for a phenomenological description of decoherence.

Finally, one should realize that within the framework of DFT, both XC potential and XC kernel are needed to calculate the dielectric function in frequency domain, while only XC potential is needed in time domain. In principle, XC potential and XC kernel are both nonlocal in time and space, so they are very complicated. In practice, it needs approximations for the accurate time-dependent XC potential and XC kernel with nonlocality in space and time, and the property of derivative discontinuity. Based on the above points, the calculation of the dielectric function in a time domain will introduce less error than that in a frequency domain.

IV. CONCLUSIONS

In conclusion, on the one hand, by introducing polarization density, a small improvement of the dielectric function approach can unify the treatment of longitudinal and transverse

macroscopic geometries on the same footing. Moreover, the improvement makes the approach of calculating dielectric function more robust for the avoidance of numerical divergencies at low frequency near zero in some specific cases. On the other hand, we conduct a numerical study of an improved real-time current-based approach for calculating the dielectric function of bulk periodic system, in which a phenomenological description of decoherence has been incorporated within the framework of TDDFT. Taking bulk diamond and silicon as examples, with allowance for the decoherence, we have verified the validity of the improvement implementation at the level of real-time TDDFT dielectric function calculations in the ground state by comparing with the corresponding experimental result. It is concluded that the decoherence TDDFT model can suppress the numerical divergence of low fre-

quency and grows the excitonic feature of silicon, although it adopts the approximate time-dependent XC potential, demonstrating the high promise of our decoherence TDDFT model as a tool in the arsenal of TDDFT methods. These incremental improvements are technically important and generally applicable to other theories that do not necessarily rely on TDDFT. Thus, this deserves to be investigated in future research theoretically.

ACKNOWLEDGMENTS

This work was supported by the National Natural Science Foundation of China (Grants No. 11774030, No. 51735001, and No. 52075004) and the Beijing Natural Science Foundation (Grant No. 2192049).

-
- [1] G. F. Bertsch, J. I. Iwata, A. Rubio, and K. Yabana, Real-space, real-time method for the dielectric function, *Phys. Rev. B* **62**, 7998 (2000).
- [2] P. Romaniello and P. L. de Boeij, Time-dependent current-density-functional theory for the metallic response of solids, *Phys. Rev. B* **71**, 155108 (2005).
- [3] J. Yan, K. W. Jacobsen, and K. S. Thygesen, Conventional and acoustic surface plasmons on noble metal surfaces: A time-dependent density functional theory study, *Phys. Rev. B* **86**, 241404(R) (2012).
- [4] S. A. Sato, Y. Shinohara, T. Otobe, and K. Yabana, Dielectric response of laser-excited silicon at finite electron temperature, *Phys. Rev. B* **90**, 174303 (2014).
- [5] Y. Shinohara, K. Yabana, Y. Kawashita, J.-I. Iwata, T. Otobe, and G. F. Bertsch, Coherent phonon generation in time-dependent density functional theory, *Phys. Rev. B* **82**, 155110 (2010).
- [6] S. A. Sato, K. Yabana, Y. Shinohara, T. Otobe, and G. F. Bertsch, Numerical pump-probe experiments of laser-excited silicon in nonequilibrium phase, *Phys. Rev. B* **89**, 064304 (2014).
- [7] V. U. Nazarov and G. Vignale, Optics of Semiconductors from Meta-Generalized-Gradient-Approximation-Based Time-Dependent Density-Functional Theory, *Phys. Rev. Lett.* **107**, 216402 (2011).
- [8] Y. Zempo and N. Akino, Dielectric properties of semiconductors by TDDFT in real-space and real-time approach, *MRS Online Proc. Library* **829**, 463 (2004).
- [9] T. Otobe, M. Yamagiwa, J. I. Iwata, K. Yabana, T. Nakatsukasa, and G. F. Bertsch, First-principles electron dynamics simulation for optical breakdown of dielectrics under an intense laser field, *Phys. Rev. B* **77**, 165104 (2008).
- [10] X. Q. Zhang, F. Wang, L. Jiang, and Y. Yao, Manipulation of the dielectric properties of diamond by an ultrashort laser pulse, *Phys. Rev. B* **95**, 184301 (2017).
- [11] X. Q. Zhang, F. Wang, F. Zhang, and Y. Yao, Control of the hyperbolic dispersion of dielectrics by an ultrashort laser pulse, *Phys. Rev. B* **97**, 014310 (2018).
- [12] X. Zhang, F. Wang, X. Wang, and L. Jiang, Controlling anisotropy of dielectrics by an ultrashort double-pulse laser, *J. Phys. D: Appl. Phys.* **52**, 035106 (2019).
- [13] S. A. Sato, K. Yabana, Y. Shinohara, T. Otobe, K. M. Lee, and G. F. Bertsch, Time-dependent density functional theory of high-intensity short-pulse laser irradiation on insulators, *Phys. Rev. B* **92**, 205413 (2015).
- [14] S. A. Sato and K. Yabana, Efficient basis expansion for describing linear and nonlinear electron dynamics in crystalline solids, *Phys. Rev. B* **89**, 224305 (2014).
- [15] D. Sangalli, J. A. Berger, C. Attaccalite, M. Grüning, and P. Romaniello, Optical properties of periodic systems within the current-current response framework: Pitfalls and remedies, *Phys. Rev. B* **95**, 155203 (2017).
- [16] M. Springborg and B. Kirtman, Analysis of vector potential approach for calculating linear and nonlinear responses of infinite periodic systems to a finite static external electric field, *Phys. Rev. B* **77**, 045102 (2008).
- [17] D. Sangalli, A. Marini, and A. Debernardi, Pseudopotential-based first-principles approach to the magneto-optical Kerr effect: From metals to the inclusion of local fields and excitonic effects, *Phys. Rev. B* **86**, 125139 (2012).
- [18] D. Neuhauser and R. Baer, Efficient linear-response method circumventing the exchange-correlation kernel: Theory for molecular conductance under finite bias, *J. Chem. Phys.* **123**, 204105 (2005).
- [19] K. Yabana, T. Sugiyama, Y. Shinohara, T. Otobe, and G. F. Bertsch, Time-dependent density functional theory for strong electromagnetic fields in crystalline solids, *Phys. Rev. B* **85**, 045134 (2012).
- [20] G. Wachter, C. Lemell, J. Burgdörfer, S. A. Sato, X.-M. Tong, and K. Yabana, *Ab initio* Simulation of Electrical Currents Induced by Ultrafast Laser Excitation of Dielectric Materials, *Phys. Rev. Lett.* **113**, 087401 (2014).
- [21] T. Otobe, K. Yabana, and J. Iwata, First-principles calculation of the electron dynamics in crystalline SiO₂, *J. Phys.: Condens. Matter* **21**, 064224 (2009).
- [22] C. D. Pemmaraju, F. D. Vila, J. J. Kas, S. A. Sato, J. J. Rehr, K. Yabana, and D. Prendergast, Velocity-gauge real-time TDDFT within a numerical atomic orbital basis set, *Comput. Phys. Commun.* **226**, 30 (2018).
- [23] M. Noda, S. A. Sato, Y. Hirokawa, M. Uemoto, T. Takeuchi, S. Yamada, A. Yamada, Y. Shinohara, M. Yamaguchi, K. Iida, *et al.*, SALMON: Scalable *ab-initio* light-matter simulator for

- optics and nanoscience, *Comput. Phys. Commun.* **235**, 356 (2019).
- [24] K. Yabana, T. Nakatsukasa, J.-I. Iwata, and G. Bertsch, Real-time, real-space implementation of the linear response time-dependent density-functional theory, *Phys. Status Solidi B* **243**, 1121 (2006).
- [25] Y. Takimoto, F. Vila, and J. Rehr, Real-time time-dependent density functional theory approach for frequency-dependent nonlinear optical response in photonic molecules, *J. Chem. Phys.* **127**, 154114 (2007).
- [26] X. Kong, F. Wang, X. Zhang, Z. Liu, and X. Wang, Dielectric properties of cubic boron nitride modulated by an ultrashort laser pulse, *Phys. Rev. A* **98**, 053439 (2018).
- [27] G. Wachter, S. A. Sato, I. Floss, C. Lemell, X.-M. Tong, K. Yabana, and J. Burgdörfer, Controlling ultrafast currents by the nonlinear photogalvanic effect, *New J. Phys.* **17**, 123026 (2015).
- [28] D. Neuhauser and K. Lopata, Quantum Drude friction for time-dependent density functional theory, *J. Chem. Phys.* **129**, 134106 (2008).
- [29] M. Cazzaniga, L. Caramella, N. Manini, and G. Onida, *Ab initio* intraband contributions to the optical properties of metals, *Phys. Rev. B* **82**, 035104 (2010).
- [30] C. Aversa and J. E. Sipe, Nonlinear optical susceptibilities of semiconductors: Results with a length-gauge analysis, *Phys. Rev. B* **52**, 14636 (1995).
- [31] M. S. Wismer, M. I. Stockman, and V. S. Yakovlev, Ultrafast optical Faraday effect in transparent solids, *Phys. Rev. B* **96**, 224301 (2017).
- [32] K. Yabana and G. F. Bertsch, Time-dependent local-density approximation in real time: Application to conjugated molecules, *Int. J. Quantum Chem.* **75**, 55 (1999).
- [33] M. Petersilka and E. K. U. Gross, Strong-field double ionization of helium: A density-functional perspective, *Laser Phys.* **9**, 105 (1999).
- [34] A. K. Dhara and S. K. Ghosh, Density-functional theory for time-dependent systems, *Phys. Rev. A* **35**, 442 (1987).
- [35] S. K. Ghosh and A. K. Dhara, Density-functional theory of many-electron systems subjected to time-dependent electric and magnetic fields, *Phys. Rev. A* **38**, 1149 (1988).
- [36] N. Troullier and J. L. Martins, Efficient pseudopotentials for plane-wave calculations, *Phys. Rev. B* **43**, 1993 (1991).
- [37] N. T. Maitra, I. Souza, and K. Burke, Current-density functional theory of the response of solids, *Phys. Rev. B* **68**, 045109 (2003).
- [38] S. Yamada, M. Noda, K. Nobusada, and K. Yabana, Time-dependent density functional theory for interaction of ultrashort light pulse with thin materials, *Phys. Rev. B* **98**, 245147 (2018).
- [39] M. D. Tokman, Gauge invariance of phenomenological models of the interaction of quantum dissipative systems with electromagnetic fields, *Phys. Rev. A* **79**, 053415 (2009).
- [40] M. A. Marques, A. Castro, G. F. Bertsch, and A. Rubio, octopus: A first-principles tool for excited electron-ion dynamics, *Comput. Phys. Commun.* **151**, 60 (2003).
- [41] A. Castro, H. Appel, M. Oliveira, C. A. Rozzi, X. Andrade, F. Lorenzen, M. A. Marques, E. Gross, and A. Rubio, *octopus*: A tool for the application of time-dependent density functional theory, *Phys. Status Solidi B* **243**, 2465 (2006).
- [42] J. P. Perdew, A. Ruzsinszky, G. I. Csonka, O. A. Vydrov, G. E. Scuseria, L. A. Constantin, X. Zhou, and K. Burke, Restoring the Density-Gradient Expansion for Exchange in Solids and Surfaces, *Phys. Rev. Lett.* **100**, 136406 (2008).
- [43] A. Castro, M. A. Marques, and A. Rubio, Propagators for the time-dependent Kohn-Sham equations, *J. Chem. Phys.* **121**, 3425 (2004).
- [44] H. R. Philipp and E. A. Taft, Optical properties of diamond in the vacuum ultraviolet, *Phys. Rev.* **127**, 159 (1962).
- [45] E. D. Palik, editor, *Handbook of Optical Constants of Solids* (Academic Press, New York, 1985).
- [46] W. Ku and A. G. Egiluz, Band-Gap Problem in Semiconductors Revisited: Effects of Core States and Many-Body Self-consistency, *Phys. Rev. Lett.* **89**, 126401 (2002).
- [47] S. Albrecht, L. Reining, R. Del Sole, and G. Onida, *Ab initio* Calculation of Excitonic Effects in the Optical Spectra of Semiconductors, *Phys. Rev. Lett.* **80**, 4510 (1998).
- [48] E. K. U. Gross and W. Kohn, Local Density-Functional Theory of Frequency-Dependent Linear Response, *Phys. Rev. Lett.* **55**, 2850 (1985).
- [49] S. Sharma, J. K. Dewhurst, A. Sanna, and E. K. U. Gross, Bootstrap Approximation for the Exchange-Correlation Kernel of Time-Dependent Density-Functional Theory, *Phys. Rev. Lett.* **107**, 186401 (2011).
- [50] P. E. Trevisanutto, A. Terentjevs, L. A. Constantin, V. Olevano, and F. D. Sala, Optical spectra of solids obtained by time-dependent density functional theory with the jellium-with-gap-model exchange-correlation kernel, *Phys. Rev. B* **87**, 205143 (2013).
- [51] S. Cavo, J. A. Berger, and P. Romaniello, Accurate optical spectra of solids from pure time-dependent density functional theory, *Phys. Rev. B* **101**, 115109 (2020).
- [52] J. A. Berger, Fully Parameter-Free Calculation of Optical Spectra for Insulators, Semiconductors, and Metals from a Simple Polarization Functional, *Phys. Rev. Lett.* **115**, 137402 (2015).